Author(s): López-Estrada, Omar; Mammen, Nisha; Laverdure, Laura; Melander, Marko M.; Häkkinen, Hannu; Honkala, Karoliina

Title: Computational Criteria for Hydrogen Evolution Activity on Ligand-Protected Au25-Based Nanoclusters

Year: 2023

Version: Published version

Please cite the original version:

López-Estrada, O., Mammen, N., Laverdure, L., Melander, M. M., Häkkinen, H., & Honkala, K. (2023). Computational Criteria for Hydrogen Evolution Activity on Ligand-Protected Au25-Based Nanoclusters. ACS Catalysis, 13(13), 8997-9006. https://doi.org/10.1021/acscatal.3c01065

ACS Catalysis

pubs.acs.org/acscatalysis Research Article

Computational Criteria for Hydrogen Evolution Activity on Ligand-Protected Au_{25}-Based Nanoclusters

Omar López-Estrada, Nisha Mammen, Laura Laverdure, Marko M. Melander, Hannu Häkkinen,* and Karoliina Honkala*

Cite This: *ACS Catal.* 2023, 13, 8997−9006 Read Online

ACCESS | Metrics & More | Article Recommendations | Supporting Information

ABSTRACT: The hydrogen evolution reaction (HER) is a critical reaction in addressing climate change; however, it requires catalysts to be generated on an industrial scale. Nanomaterials offer several advantages over conventional HER catalysts, including the possibility of atomic precision in tailoring the intrinsic activity. Ligand-protected metal clusters, such as the thiolate-protected $MAu_{24}(SR)_{18}$ (where M is Au, Cu, Pd), are of particular interest as not only are they electrocatalytically active toward HER, but the charge state and composition can be precisely tuned. Here, we present a comprehensive computational study examining how the charge state and dopants affect the catalytic activity of $[MAu_{24}(SCH_3)_{18}]^q$ toward the Volmer step of the HER. Assuming an adsorbed hydrogen atom to be the key intermediate, then, according to the Sabatier principle, the H adsorption energy should be nearly thermoneutral for an ideal HER catalyst. Our results show that adsorption energies alone are an insufficient criterion to identify a promising catalytic material; experimentally relevant redox potentials, the corresponding catalyst's charge states, and the kinetic barriers should also be considered. Notably, this work explains the relative activity of $MAu_{24}(SR)_{18}$ (M = Au, Cu, Pd) clusters reported by Kumar et al. (*Nanoscale* **2020**, *12*, 9969). Our results validate a more thorough computational approach that includes charge and redox potential to understand and screen electrocatalytically active nanoclusters.

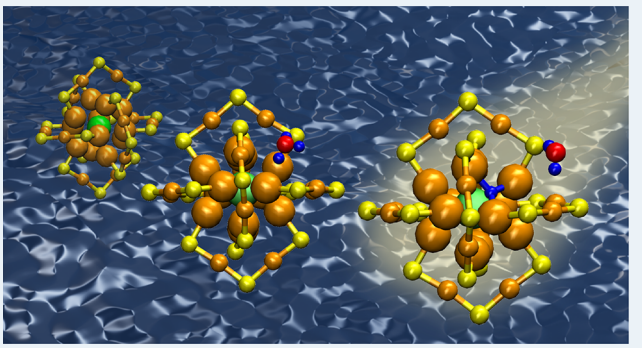

KEYWORDS: *electrocatalysis, HER, gold nanocluster, ligand protected cluster, doping, redox potential, density functional theory*

INTRODUCTION

Clean, renewable sources of energy are required to mitigate anthropogenic climate change driven by CO_2 emissions.[1,2] Current sources of clean energy such as wind and solar are intermittent and the challenge becomes one of energy storage.[2] An attractive solution to this problem is to use hydrogen produced from electrocatalytic water-splitting as fuel,[3,4] due to its high mass energy density.[5] Water-splitting consists of two half-reactions, namely the oxygen evolution reaction (OER) and the hydrogen evolution reaction (HER).[4] The HER is a two-electron transfer reaction that occurs in two steps. The possibilities under acidic conditions are as follows:

$$H^+ + e^- + {}^* \rightarrow H^* \qquad \text{Volmer step}$$

$$H^* + H^+ + e^- + {}^* \rightarrow H_2 + {}^* \qquad \text{Heyrovsky step}$$

$$2H^* \rightarrow H_2 + 2^* \qquad \text{Tafel step}$$

These three reaction steps form the two possible HER mechanisms: the Volmer−Heyrovsky mechanism and the Volmer−Tafel mechanism. According to the Sabatier principle,[6] a good HER catalyst does not bind the hydrogen too weakly or too strongly.[7] The rate of the overall reaction is determined by the Volmer step for a weakly adsorbed hydrogen atom and by the Heyrovsky/Tafel step for a strongly adsorbed hydrogen atom.[8] Optimized electrocatalysts are required to achieve the efficiency necessary for industrial-scale hydrogen production.[9,10] Currently, Pt is still the best HER catalyst under acidic conditions.[11,12] Limited improvements in this material's activity can made by roughening the surface to expose more active sites or by increasing the catalyst loading.[13] Therefore, there is a strong impetus to improve intrinsic activity by considering other classes of materials, such as nanoparticles and nanoclusters.

The catalytic activity of protected gold nanoclusters (NCs) has been tested experimentally,[14,15] and these systems offer several advantages over conventional bulk materials such as

Received: March 8, 2023
Revised: June 5, 2023
Published: June 22, 2023

size-controllable synthesis, tailoring of the organic ligands, and high stability in solution and solid state.[16−19] Small NCs belong to the so-called "every-atom-counts region" where adding or removing a single atom alters the NC's physical and chemical properties. Furthermore, the ability to control the nanocluster's composition through doping and ligand tailoring allows structural optimization toward a specific function, in this instance, catalyzing the HER reaction.[20−22] $Au_{25}(SR)_{18}$ in particular has emerged as a promising catalyst and is one of the most widely studied atomically precise structures with its own broad crystallographic database.[22] These nanoclusters' stability as homogeneous and heterogeneous catalysts makes them highly versatile. Ligands are necessary to stabilize the metal core, and their composition can alter the cluster's overall physical and chemical properties including its stability and effective catalysis in a given solvent.[23] Doping these clusters with other metallic elements such as Pt, Pd, and Cu has also been shown to alter the cluster's physicochemical properties, for example, redox potentials, optical absorption, and reactant adsorption energies.[24−27] Doping $Au_{25}(SR)_{18}$ clusters can also modify the ground-state charge which is of particular interest for electrochemical reactions.[24,25] $Au_{25}(SR)_{18}$-based clusters can be effective electron transfer mediators when their redox potential closely matches the reactants' thermodynamic potential.[25] In particular, the clusters' redox potential in solution was found to correlate well with the potential at which HER activity is detected on the solid electrode.[27] The charge state, electrode potential, and catalyst activity are strongly correlated; therefore, meaningful calculations on $Au_{25}(SR)_{18}$ clusters' HER activity should ensure the clusters have the correct charge state at potentials used for HER experimentally.

Previous computational studies have quantified NC-catalyzed HER activity in terms of hydrogen adsorption energies and the Sabatier principle, linking the adsorption energy with the exchange current to construct volcano plots. This analysis, based on thermodynamic quantities, has been widely used to screen for HER catalysts to avoid explicitly calculating reaction kinetics. While previous studies have investigated pure and doped $Au_{25}(SR)_{18}$ clusters' HER activity by following the Sabatier principle and computing hydrogen adsorption energies, there are concerns that a nearly thermoneutral hydrogen adsorption energy is insufficient to explain HER activity.[28−31] Furthermore, adsorption energies are typically computed for the cluster's most stable charge state which does not necessarily correspond to the charge state found under experimental conditions that is, at a given electrode potential.[24,27,32] To correctly account for the electrode potential in DFT simulations, calculations should be performed using constant potential, Grand Canonical ensemble DFT.[33,34] This would, however, be extremely costly computationally, as both the NC and the electrode onto which it is deposited must be explicitly simulated. An equally rigorous alternative is to use canonical, fixed-charge DFT with the charge state that occurs at the desired potential.[33,34]

In this work, we investigate HER thermodynamics and kinetics by examining the Volmer step in $[MAu_{24}(SR)_{18}]^q$ (M = Au, Pd, Cu) NCs. This reaction step is necessary in the two possible mechanisms for HER. While the Volmer step is also the rate-determining step on Au(111),[28,35] the mechanistic details for HER on $Au_{25}(SR)_{18}$-based clusters remain unclear. For example, on $Au_{25}(SR)_{18}$, a Tafel slope of ∼70 mV dec^{-1} was extracted from from Kumar et al.'s experimental data.[26] Tafel slopes depend on several parameters including the coverage of H atoms on the catalyst's surface as shown by previous studies.[36] In this study, we assume low coverage due to endergonic hydrogen adsorption energies. At low coverages, the expected slopes for the Volmer, Heyrovsky, or Tafel step being rate-determining were estimated to be 120, 40, and 30 mV dec^{-1}, respectively.[37] Cu and Pd were selected as dopants because experiments have shown that they represent extremes in the HER performance of doped $Au_{25}SR_{18}$ nanoclusters. The onset potentials for HER activity, corresponding to the foot-of-the-wave in the linear sweep voltammogram, follow the order: $PdAu_{24}$ < Au_{25} < $CuAu_{24}$. Specifically, at any given potential, Pd exhibited the highest current density while Cu exhibited the lowest.[26] We study the stability of the nanoclusters by correlating the superatomic electronic structure and the HOMO−LUMO gap (where HOMO is the highest occupied molecular orbital and LUMO is the lowest unoccupied molecular orbital) of five different charge states (q = −2, −1, 0, +1, +2). Redox potentials were calculated to establish the relevant charge states for electrode potentials used in the HER. Adsorption energies for 1−3 H atoms are tested as a simple thermodynamic descriptor to identify clusters that may exhibit high HER activity. In addition, by studying the adsorption energetics of more than 1 H, we can make inferences about the overall mechanism and whether multiple HER sites on a single NC are possible. By computing free energies of reaction and activation for the Volmer step under acidic conditions, we are able to show that H adsorption energies on nanoclusters based on $[Au_{25}(SCH_3)_{18}]^q$ do not have as linear a correlation with activation barriers as expected in Brønsted−Evans−Polanyi analyses. In addition, the computed kinetic barriers for the first Volmer step on some $[MAu_{24}(SR)_{18}]^q$ (M = Au, Pd, Cu) clusters are comparable to those calculated on Pt,[28,38] which is known to be one of the best HER catalysts. This implies that ligand-protected, doped gold clusters have great potential as promising HER electrode materials.

COMPUTATIONAL DETAILS

The molecular structures used in this study are based on the crystallographic data provided by Tofanelli et al.,[39] where the 2-phenylethanethiol ligands are substituted with methylthiol groups. This truncation was done to lower computational costs and reduce the configurational space. All spin-polarized ground-state computations were performed employing the real-space grid base GPAW software.[40−42] The frozen core PAW approximation was used for all the elements, with 16, 11, 11, 6, 6, 4, and 1 valence electrons for Pd, Au, Cu, S, O, C and H, respectively. The exchange correlation effects were considered employing the GGA-PBE[43] functional with the Tkatchenko−Scheffler dispersion correction.[44] Smearing of electron occupations was set to zero to prevent the fractional occupation of states.

All calculations were carried out using a cubic cell of dimensions 28.8 Å × 28.8 Å × 28.8 Å, with a real-space grid spacing of 0.2 Å. The water solvent effect was included by employing a continuum solvent model[45] as implemented in GPAW. The optimization was finished when the residual forces on each atom were less than 0.05 eV/Å.

To associate the electrode potential with the correct charge, we calculated the redox potential using the Nernst equation:

$$E^{\circ}_{R/O} = -\frac{\Delta G^{\circ}_{R/O}}{n_e F} - E^{\circ}_{ABS}(REF) \quad (1)$$

https://doi.org/10.1021/acscatal.3c01065
ACS Catal. 2023, 13, 8997−9006

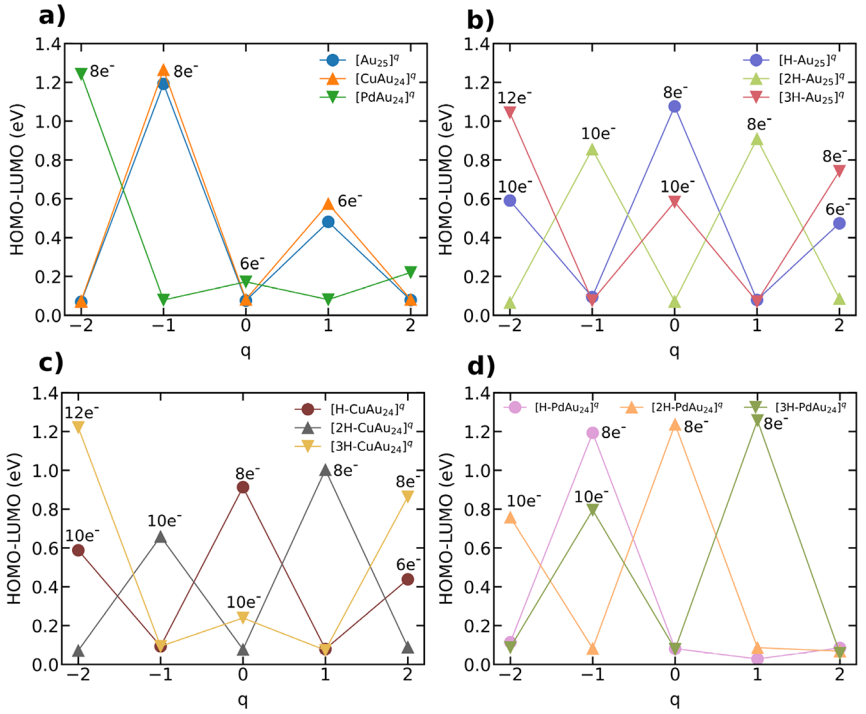

Figure 1. HOMO−LUMO gap (eV) for $[Au_{25}(SR)_{18}]^q$, $[CuAu_{24}(SR)_{18}]^q$ and $[PdAu_{24}(SR)_{18}]^q$ clusters, and n adsorbed hydrogen atoms on each cluster with charges, q = −2, −1, 0, 1, 2 and n = 1−3. The number of superatomic electrons is indicated for the most stable structures.

where $\Delta G^{\circ}_{R/O}$ is the free energy of the reduction or oxidation process under standard conditions, n_e the number of electrons transferred in the process, and F the Faraday constant. The first term gives the redox potential on an absolute scale; the second term, E°_{ABS}(REF), is the SHE (Standard Hydrogen Electrode) potential on the absolute scale, which has been determined to be 4.44 V.[46] The free energy of reduction or oxidation is calculated according to

$$\Delta G^{\circ}_{R/O} = IP + \Delta G^{\circ}_{trans,vib,rot,ZPE} + \Delta\delta G^{\circ}_{solv} \quad (2)$$

where IP is the vertical ionization energy from $[M_xAu_{25-x}]^q \rightarrow [M_xAu_{25-x}]^{q+1}$. The difference in the translational, vibrational, rotational, and zero-point energy contributions to the free energy of the two charge states involved is given by $\Delta G^{\circ}_{trans,vib,rot,ZPE}$. This term is expected to be negligible because the structural differences that accompany the change in the charge state are minor (Figure SI-1 in the Supporting Information). It is also neglected as even using a rigid-rotor harmonic oscillator approximation to obtain this quantity is too computationally burdensome. The last term, $\Delta\delta G^{\circ}_{solv}$, represents differences in solvation energy, that is, the energy spent as solvent molecules rearrange around the newly charged species. Although we do not consider explicit solvation to keep the model simple and the computational expense manageable, the change in solvation energy is partially accounted for with a continuum solvation model.

Adsorption energies E_b for n hydrogen atoms on pure and doped clusters were calculated according to

$$E_b = E(Au + nH) - E(Au + (n-1)H) - \frac{1}{2}E(H_2) \quad (3)$$

where $E(Au + nH)$ and $E(Au + (n-1)H)$ are the potential energies of the system with n and $n-1$ adsorbed H atoms, respectively, and $E(H_2)$ is the energy of the gas-phase H_2 molecule.

The free energies of reaction and activation for the first and second Volmer steps on these clusters were determined for the following reactions:

$$H_3O^+ + [MAu_{24}(SR)_{18}]^{q-1} \rightarrow H_2O + [HMAu_{24}(SR)_{18}]^q \quad (4)$$

$$H_3O^+ + [HMAu_{24}(SR)_{18}]^{q-1} \rightarrow H_2O + [H_2MAu_{24}(SR)_{18}]^q \quad (5)$$

where M = Au, Cu, Pd, and q = −1, 0, +1, and +2. To determine kinetic energy barriers, transition states were identified with the climbing image nudged elastic band method,[47,48] using five images and a convergence criterion of 0.05 eV/Å. We performed Bader charge analysis[49] to validate the local charge on the nanocluster, H and H_3O^+ for every initial, transition, and final state identified.

A limited vibrational analysis was performed to confirm stationary states as minima or transition states and to compute the structures' free energies by obtaining the zero point energies and entropic contributions. Only the vibrational contributions from the H_3O^+, H_2O, and adsorbed H in the reaction systems are considered in the calculations as the entropic contribution from the NC's vibrational modes is expected to be negligible. The free energies of reaction and activation reported herein were calculated as the difference between the products and reactants in the same unit cell.

RESULTS AND DISCUSSION

We explored the energetics and Au core distortions of the $[MAu_{24}(SCH_3)_{18}]$ structures, which were optimized as described in the computational section at different charge states, q = −2, −1, 0, +1, +2. Distances between the central

https://doi.org/10.1021/acscatal.3c01065
ACS Catal. 2023, 13, 8997−9006

atom and icosahedral surface atoms vary from 2.81 Å to 2.92 Å, in agreement with previous reports for $Au_{25}(PET)_{18}^{(-1,0,1)}$,[39] which show that these distances vary between 2.7 Å and 3.3 Å. To illustrate structural distortions caused by the charge state, we examined the clusters' overlap with $[Au_{25}(SCH_3)_{18}]^{-2}$, which is used as a reference. As can be seen in Figure SI-1, there are no significant structural differences between $[Au_{25}(SR)_{18}]^q$ clusters with different charge states. The negligible structural differences between charge states agree with a previous study on $Au_{25}(PET)_{18}^{(-1,0,1)}$.[39] This observation suggests that instead of differences in relative atomic positions, purely electronic structural differences cause the clusters' varying catalytic activity.

CU- AND PD-DOPED $[AU_{25}(SR)_{18}]^Q$ CLUSTERS

We analyzed the effects of doping the $[Au_{25}(SCH_3)_{18}]$ structure with Cu or Pd for each charge state. For the sake of clarity, we adopt a notation of $[Au_{25}]^q$, $[CuAu_{24}]^q$, $[Cu_2Au_{23}]^q$, and $[PdAu_{24}]^q$ to refer to the nanocluster systems and their charge states (q = −2, −1, 0, +1, +2). Three symmetrically nonequivalent positions for Cu and Pd-doping are identified as the center of the icosahedral core, the surface of the icosahedron, and part of the S−Au−S staple motif (Figure SI-2 in the Supporting Information). Fractional, although greater than 1, Cu-doping reported experimentally[50,51] raises the possibility of a double Cu substitution. We therefore investigated the double substitution of two Au atoms with Cu atoms for several different possible combinations of positions in the $[Au_{25}]^q$ clusters, as shown in Figure SI-3 in the Supporting Information. The relative energies for the $[CuAu_{24}]^q$, $[Cu_2Au_{23}]^q$, and $[PdAu_{24}]^q$ NCs are summarized in Tables SI-2−SI-4, respectively, in the Supporting Information.

To compare the electronic stability of the pure Au cluster with its Cu and Pd-doped counterparts, we correlate the HOMO−LUMO gaps with the superatom's[52] electron configuration and overall charge (see Figure 1a). Large (small) HOMO−LUMO gaps indicate a greater (lesser) electronic stability. The $[Au_{25}(SR)_{18}]^q$ electronic structure configurations have been extensively studied with different thiol ligands and charge states. The superatomic electron counting rule[52] considers the valence electrons donated/withdrawn by the metal atoms/thiols to/from the cluster's metallic core. The $[Au_{25}(SR)_{18}]^{-1}$ system has been widely reported as having an $8e^-$ superatomic configuration ($1S^21P^6$), where each Au contributes $1e^-$ and each thiol withdraws $1e^-$.[53] Additionally, a recent study reported that hydrogen adsorbed to the metal core of Au_{25}-based nanoclusters also behaves as a metal and thus contributes its 1s electron to the superatom's electronic configuration.[24] Table SI-1 in the Supporting Information summarizes the different superatomic electron configurations. As expected, our calculations show that the $[Au_{25}]^{-1}$ cluster is the most stable with a HOMO−LUMO gap of 1.19 eV due to the closure of the core−shell with an eight-electron superatomic configuration (Figure 1a). Also expected, $[Au_{25}]^{+1}$ NC is the second-most stable with a six-electron superatomic configuration ($1S^21P^4$) and a gap of 0.48 eV. The $[Au_{25}]$ NCs with q = +2, 0, −2 each have an odd number of superatomic electrons and have much smaller HOMO−LUMO gaps, between 0.07−0.08 eV. The order of electronic stability is therefore −1 > +1 > +2 > 0 > −2.

The relative energies of a single Cu-dopant at the center, on the surface of the icosahedral core or in one of the S−Au−S staple motifs are found in the range of 11−108 meV, regardless of the charge state (see Table SI-3). The range of relative energies is wider for $[Cu_2Au_{23}]$ NCs than for $[CuAu_{24}]$ NCs; however, it is still much smaller than that observed for $[PdAu_{24}]$ NCs. Although experiments have shown Cu to preferentially substitute for Au atoms in staple positions,[50,51] our results suggest the different isomers are energetically competitive and therefore the site preference observed experimentally must be due to low kinetic barriers encountered in the synthesis. To reduce the configurational space, we study H adsorption and HER energetics using only the lowest energy structures with a single dopant atom for each charge state. The doubly doped NCs will only be used to evaluate the redox potentials.

As with Au, the Cu atom donates its 1s electron to the core, and the $8e^-$ superatom is $[CuAu_{24}]^{-1}$. $[CuAu_{24}]^{-1}$ is the most stable charge state, similar to the pure NC, with a HOMO−LUMO gap of 1.27 eV (Table SI-2). This Cu-doped cluster substitutes for an Au atom on the surface of the icosahedral core and its HOMO−LUMO gap is 73 meV larger than its pure Au counterpart. As observed in the pure Au NC, the second-most stable Cu-doped cluster corresponds to the $6e^-$ superatom, $[CuAu_{24}]^{+1}$, with a HOMO−LUMO gap of 0.58 eV. The $[CuAu_{24}]$ NCs with an odd number of superatomic electrons also have smaller band gaps, between 0.07 and 0.08 eV, than those with an even number of superatomic electrons. Cu substitutes an Au atom on the surface of the icosahedron core for the $8e^-$ $[CuAu_{24}]^{-1}$, $6e^-$ $[CuAu_{24}]^{+1}$, and $5e^-$ $[CuAu_{24}]^{+2}$ clusters, whereas it substitutes the central Au atom for the $9e^-$ $[CuAu_{24}]^{-2}$ and $7e^-$ $[CuAu_{24}]^0$ NCs (see Table SI-3). The order of stability for these systems is −1 > +1 > 0, +2 > −2.

Previous experimental and computational studies have shown that Pd preferentially substitutes the central Au atom in the Au_{13} icosahedron.[54−58] Our calculations agree with this finding and show that this preferred doping site is independent of the charge state (Table SI-2). According to the superatomic electron counting rules, Pd does not donate a valence electron; therefore, $[PdAu_{24}]^{-2}$ achieves the $1S^21P^6$ superatomic configuration of eight electrons (see Table SI-2 and Figure 1a). The $8e^-$ $[PdAu_{24}]^{-2}$ NC exhibits the highest HOMO−LUMO gap, 1.24 eV, among all the different charge states (see Table SI-2) and is electronically more stable than its $[Au_{25}]^{-1}$ counterpart by 50 meV. Interestingly, the $4e^-$ $[PdAu_{24}]^{+2}$ NC is more stable than the $6e^-$ $[PdAu_{24}]^0$ NC by 48 meV as seen by the HOMO−LUMO gap (see Table SI-2). The stability trend for these NCs is then −2 > +2 > 0 > +1 > −1.

REDOX POTENTIALS

Monoatomically doping the $[Au_{25}]^{-1}$ cluster changes the electronic structure and opens the possibility to tune the redox potentials and, hence, lower the overpotentials encountered for HER. Our calculated redox potentials shown in Table 1 are in good agreement with experimental values found for the −2/−1 redox pairs, −1.476 V_{SHE} (Au_{25}), − 1.272 V_{SHE} ($CuAu_{24}$), and −0.476 V_{SHE} ($PdAu_{24}$).[27,50,59] As the charge state increases, however, the deviation in our calculated redox potentials from experimental values increases. These deviations may be caused by errors in the difference in solvation energies. Deficiencies in the solvation model have been shown to overshadow any gains in accuracy that may be achieved using a higher level of theory.[60] Deviations from experiment may also be the result of the ligand truncation, as the experimental values taken for comparison are from clusters with bulkier 2-phenylethanethiol

https://doi.org/10.1021/acscatal.3c01065
ACS Catal. 2023, 13, 8997−9006

Table 1. Redox Potentials (V_{SHE}) for $[Au_{25}(SR)_{18}]^q$, $[CuAu_{24}(SR)_{18}]^q$, $[Cu_2Au_{23}(SR)_{18}]^q$ and $[PdAu_{24}(SR)_{18}]^q$ Clusters with Reduced $q = -2, -1, 0, 1, 2$

	Redox potential (V_{SHE})			
redox pair	Au_{25}	$CuAu_{24}$	Cu_2Au_{23}	$PdAu_{24}$
−2/−1	−1.55	−1.48	−1.48	−0.55
−1/0	−0.30	−0.35	−0.31	−0.38
0/+1	−0.15	−0.16	−0.17	0.06
+1/+2	0.23	0.14	0.42	0.26
+2/+3	0.38	0.40	0.42	0.65

ligands. Indeed, Kumar et al. showed that thinner ligand layers would increase the HER current density for a given potential.[26] Nevertheless, certain qualitative trends remain; for example, redox potentials for $CuAu_{24}$ are similar to those for Au_{25} and the range of potentials observed for $PdAu_{24}$ redox pairs is much smaller than for Au_{25}. Interestingly, the redox potentials for Cu_2Au_{23} are similar to those of $CuAu_{24}$, suggesting similar electrocatalytic properties and, therefore, further justifies excluding Cu_2Au_{23} clusters from further calculations. We focus our analysis on the voltage range between 0 and −1 V_{SHE}. This extended range can help identify clusters that may have high HER activity within the margins of error afforded by the computational methods and also explain the activity on clusters that are deemed to be poor catalysts. In this range, the relevant charge states for $PdAu_{24}$ are 0, −1, and −2, while the relevant charge states for Au_{25} and $CuAu_{24}$, are +1, 0, and −1. The potentials of zero charge, that is the redox potentials that stabilize clusters with zero charge, are −0.15−0.16, and 0.06 V, respectively for Au, Cu-doped, and Pd-doped clusters. Interestingly, this follows the trend in the experimentally measured onset potentials, suggesting that the potential of zero charge is a descriptor for HER.[30] The redox potential is a relatively simple quantity to calculate that, in this case, explains the trend in activity; however, it is not a sufficient criterion to explain HER activity.

HYDROGEN ADSORPTION AND ELECTRONIC STABILITY

We studied hydrogen adsorption in pure and single-atom Cu- and Pd-doped $[Au_{25}]^q$. Different adsorption sites shown in Figure 2 and combinations thereof were explored using the lowest energy structures of the pure and doped $[Au_{25}]^q$ NC. For the first H, adsorption at a hollow site for $q = 0$, +1, and +2 is preferred, while a bridging position between two icosahedral atoms is energetically more favorable for $q = -1$ and −2, for

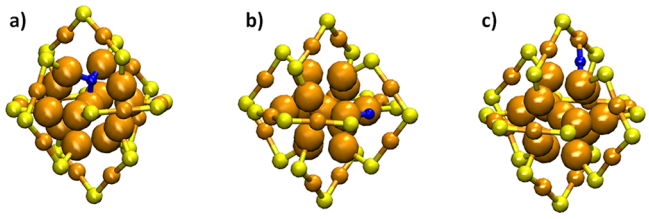

Figure 2. Hydrogen adsorption sites for the $[Au_{25}(SR)_{18}]^q$ clusters. Au atoms are represented in orange, S in yellow, and H in blue. CH_3 groups are omitted for clarity: (a) the hollow site where H binds to the central atom and two icosahedral atoms, (b) a bridge site where H is between two icosahedral atoms, and (c) another bridge site where H is between an atom in the staple motif and an icosahedral atom.

both pure and doped Au clusters. To reduce configurational space, combinations of adsorption sites for two and three adsorbed H are restricted to those where the adsorbed H is in relative proximity to each other such that H_2 may be formed later. Adsorption energies (E_b) for 1−3 H atoms at different sites are summarized in Tables SI-5−SI-7 in the Supporting Information. The lowest adsorption energies obtained for each system are presented as a function of the cluster's charge in Figure 3.

In general, hydrogen adsorbed on doped systems achieving 8 or at least an even number of superatomic electrons is more stable. Considering clusters with the same superatomic electron configuration (i.e., $[Au_{25}]^q$, $[CuAu_{24}]^q$, and $[PdAu_{25}]^{q-1}$), one can observe the following trend in adsorption energies: Au > Cu > Pd, in agreement with hydrogen adsorption observed on the corresponding metal slabs. The lowest binding energies are found when the H−Cu or H−Pd distances are smallest. In Cu-doped systems, the distances to the gold atoms involved are also shorter, but this effect is less significant. Additionally, the hydrogen preferentially adsorbs at sites closer to the nanocluster's core rather than on the surface. This suggests that the nanocluster's metal atoms and the Cu and Pd dopants in particular participate in the adsorption.

In most cases, H adsorbs endothermically into the cluster, indicating weaker binding. The charge states with adsorption energies close to zero may be promising HER catalyst candidates. The following charge states may be considered for HER catalysis due to their low adsorption energies (below ∼0.4 eV) for the first hydrogen: $q = -2$, 0, 1, and 2 for Au_{25} and $CuAu_{24}$, and $q = -1$, 0, 1, and 2 for $PdAu_{24}$. Four characteristic distances for each H atom adsorbed are distinguished: the distance between the H and the two nearest icosahedral metal atoms, the central atom, and the nearest metal atom in the staple motif. These characteristic distances for the structures with the lowest adsorption energy are summarized in Tables SI-8−SI-10 in the Supporting Information.

For Au_{25} NCs, we observe an inverse correlation between the adsorption energies and the HOMO−LUMO gaps that persists for each charge state and can be related to the superatom model. As previously mentioned, the H atom contributes its 1s electron to the superatom's electronic structure. Consequently, the $8e^-$ superatomic electron configuration shifts toward more positive charge states as the number of adsorbed H increases, regardless of the system, as can be seen in Figures 1b−d. Alternatively, higher angular momentum electronic shells are filled as the number of adsorbed hydrogens increases for a given charge state. For example, $[Au_{25}]^{-1}$, $[HAu_{25}]^0$, $[H_2Au_{25}]^{+1}$, and $[H_3Au_{25}]^{+2}$ are isoelectronic with 8 superatomic electrons. The electronic stability of these systems decreases as the number of adsorbed H increases, as indicated by HOMO−LUMO gaps of 1.19 eV ($[Au_{25}]^{-1}$), 1.09 eV ($[HAu_{25}]^0$), 0.91 eV ($[H_2Au_{25}]^{+1}$), and 0.74 eV ($[H_3Au_{25}]^{+2}$). It is notable that the difference in the HOMO−LUMO gaps for $[H_3Au_{25}]^{-2}$ and $[HAu_{25}]^{-1}$ is only 0.03 eV, indicating that higher densities of adsorbed H stabilize highly anionic Au NCs. Au_{25} NCs with an even number of superatomic electrons have larger HOMO−LUMO gaps and lower H adsorption energies. Conversely, Au_{25} NCs with an odd number of superatomic electrons have smaller HOMO−LUMO gaps and higher H adsorption energies. These observations are in agreement with and an extension to

https://doi.org/10.1021/acscatal.3c01065
ACS Catal. 2023, 13, 8997−9006

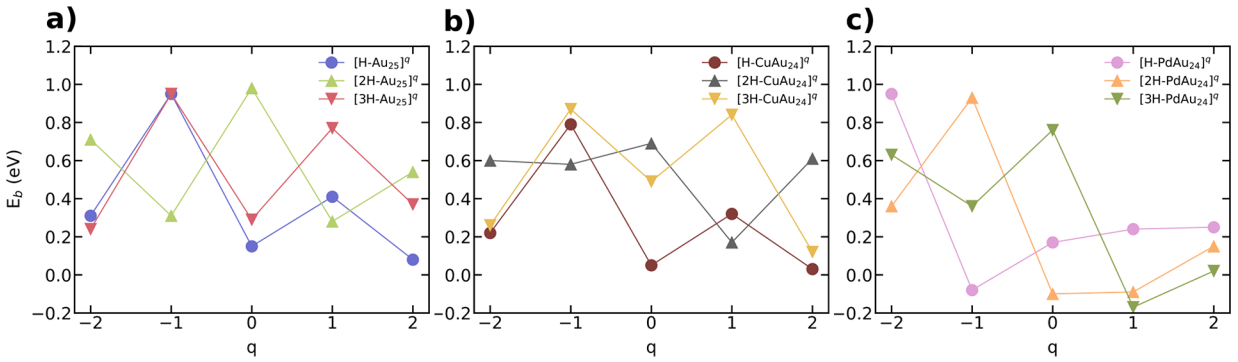

Figure 3. Adsorption energy, E_b (eV) for the nth hydrogen atom on $[Au_{25}(SR)_{18}]^q$, $[(Cu,Pd)Au_{24}(SR)_{18}]^q$ clusters where $q = -2, -1, 0, 1, 2$, and $n = 1-3$.

previous computational studies that were done on Au_{25} NCs with $q = -1, 0, +1$.[24]

The trends in the HOMO−LUMO gaps and H adsorption energies for $[CuAu_{24}]^q$ NCs are similar to those observed for $[Au_{25}]^q$ NCs, as can be seen upon comparing Figure 1c and Figure 2b. Compared to the $[Au_{25}]^q$ NCs discussed above, there is less symmetry in the HOMO−LUMO gaps and adsorption energies in the $q = 0$ charge state. The $8e^-$ systems, $[HCuAu_{24}]^0$, $[H_2CuAu_{24}]^{+1}$, and $[H_3CuAu_{24}]^{+2}$, have similar HOMO−LUMO gaps (0.91 eV, 1.00 eV, and 0.86 eV, respectively). The lowest adsorption energies for the first and third H adsorbed are found at $q = +2$, while the lowest adsorption energy for the second H is found at $q = +1$.

The $[PdAu_{24}]^q$ NCs exhibit different trends in the HOMO−LUMO gaps and H adsorption energies compared with their pure Au and Cu-doped counterparts. As shown in Figure 1d, the $8e^-$ $[PdAu_{24}]$ systems have HOMO−LUMO gaps within 0.06 eV of each other and have the following order of electronic stability: $[3H\text{-}PdAu_{24}]^{+1}$ > $[2H\text{-}PdAu_{24}]^0$ > $[1H\text{-}PdAu_{24}]^{-1}$. Figure 2c shows that these charge states also exhibit the lowest adsorption energies for the third, second, and first adsorbed hydrogen, respectively. The $10e^-$ systems, $[3H\text{-}PdAu_{24}]^{-1}$ and $[2H\text{-}PdAu_{24}]^{-2}$, are ∼0.4 eV less stable than their $8e^-$ counterparts.

VOLMER STEP ENERGETICS

Conventionally, superior activity of candidate HER catalysts has been inferred using the Sabatier principle, whereby hydrogen adsorption, that is the Volmer step, should be nearly thermoneutral.[7,28] However, optimal adsorption energies corresponding to maximum current density will shift, depending on the overall kinetics and the electrode potential.[61] To correctly account for the electrode potential, calculations should be performed using constant potential, Grand Canonical ensemble DFT.[33,34] Although many of the clusters in this study have low adsorption energies suggesting that high HER activity, kinetic parameters, such as the frequency factor and activation energy, control a catalyst's activity.[62] Therefore, to verify the clusters' activity, we investigate the free energies of reaction and activation for the first Volmer step under acidic conditions, that is, the decomposition of H_3O^+ into a proton adsorbed onto the $[MAu_{24}]^q$ cluster and a water molecule. Given the redox potentials discussed above, only the 0, −1, and −2 charge states for $PdAu_{24}$ and the +1, 0, and −1 charge states for $CuAu_{24}$ and Au_{25} need be considered, because they occur at potentials relevant for HER. For the sake of completeness, however, we report our results for all charges considered.

The calculated free energies of the reaction and activation barriers for the first Volmer step are given in Table 2. The free-energy diagrams for this reaction on each cluster are given in Figure SI-4 in the Supporting Information. We note that these results were calculated under conditions of constant charge, where q in Table 2 is the overall charge in the system and therefore neglect the effect of applied potential.

Table 2. Free Energies of Activation and Reaction for the First Volmer Step: $H_3O^+ + [MAu_{24}(SR)_{18}]^{q-1} \rightarrow H_2O + [HMAu_{24}(SR)_{18}]^q$, Where M = Au, Cu, Pd, and $q = -1, 0, 1, 2$

	Free Energy (eV)					
	Au		Cu		Pd	
q	activation	reaction	activation	reaction	activation	reaction
−1	0.000	−0.656	0.000	−0.845	0.000	−0.983
0	0.092	−0.488	0.670	−0.223	0.133	−0.056
+1	0.632	−0.072	0.450	−0.111	0.508	−0.261
+2	0.830	0.285	0.444	0.014	0.330	−0.164

As a proton is transferred from H_3O^+ to the cluster, an electron is expected to transfer from the cluster to the proton. A Bader charge analysis shows that as a H moves from H_3O^+ to an adsorption site on the cluster, the charge on this atom decreases from approximately +0.5 to 0 (see Figure SI-5 in the Supporting Information). No significant charge transfer occurs toward the other atoms forming H_2O, indicating that the adsorbed proton has gained an electron from the cluster. This confirms that the H adsorption is an electrochemical step.

We also observe a common trend in the reaction energies, where the reaction becomes increasingly exergonic as the cluster is reduced. In other words, as higher negative potentials are applied, reduced charge states are stabilized, and the first step for the HER becomes more energetically favorable. Kinetic barriers then determine the activity at each charge state.

At 0 V_{SHE}, $[Au_{25}]^{+1}$ is stable and can react with H_3O^+ to form $[HAu_{25}]^{+2}$ and H_2O (see $q = +2$ in Table 2). This reaction is endothermic and has a significant kinetic barrier of 0.83 eV. $[Au_{25}]^{+1}$ may therefore be excluded as a possible HER catalyst. Additionally, this charge state is stable only until −0.15 V, at which point the cluster is reduced to $[Au_{25}]^0$. $[Au_{25}]^0$ is stable between −0.15 and −0.30 V_{SHE} and shows a favorable reaction energy of −0.07 eV. The kinetic barrier for

https://doi.org/10.1021/acscatal.3c01065
ACS Catal. 2023, 13, 8997−9006

the proton transfer is 0.63 eV. This is comparable to the barrier calculated for the same process on Au(111) (∼0.6 eV),[28] which is a poor HER catalyst. $[Au_{25}]^{-1}$ is stabilized upon lowering the potential to −0.30 V_{SHE}. This cluster has a favorable reaction energy of −0.49 eV and a kinetic barrier of 0.09 eV making it a promising HER catalyst candidate. The proton transfer is barrierless on $[Au_{25}]^{-2}$, however, this cluster is stabilized only at very high negative potentials (−1.55 V_{SHE}) and is therefore excluded from further discussion.

Similarly, based on the redox potentials, $[CuAu_{24}]^{+1}$ is stable at 0 V_{SHE} and reduces to $[CuAu_{24}]^{0}$ below −0.16 V_{SHE}. The proton transfer on both of these clusters (see q = +2 and +1 in Table 2) is not very energetically favored, and the kinetic barriers are non-negligible. Lowering the potential below −0.35 V stabilizes $[CuAu_{24}]^{-1}$, which shows a more favorable reaction energy of −0.22 eV, but also a higher kinetic barrier of 0.67 eV (see q = 0 in Table 2). Although $[CuAu_{24}]^{-2}$ exhibits a barrierless proton transfer, it is stable only at very high negative potentials outside the range of HER potentials generally employed. These results may explain why Cu-doped clusters experimentally have lower HER activity, as demonstrated by a higher negative onset potential of −0.57 V_{SHE} (−0.53 V_{RHE} at pH 0.7)[26] than Au or Pd-doped clusters.

As discussed above, $[PdAu_{24}]$ clusters stabilize at different charge states, compared to Au and Cu-doped clusters in the potential range relevant for HER. $[PdAu_{24}]^{0}$, $[PdAu_{24}]^{-1}$, and $[PdAu_{24}]^{-2}$ form at 0.06, − 0.38, and −0.55 V_{SHE}, respectively. As shown in Table 2, the first Volmer step is thermodynamically favored for all charge states. $[PdAu_{24}]^{0}$ has a barrier of 0.51 eV and is therefore unlikely to be the active catalyst. In contrast, $[PdAu_{24}]^{-1}$ and $[PdAu_{24}]^{-2}$ have low and zero barriers, respectively, suggesting that HER readily occurs below −0.38 V_{SHE}. Our results suggest higher reactivity in $[PdAu_{24}]$ clusters than Pt(111), which has a barrier of ∼0.3 eV for the Volmer step,[28] making these clusters promising HER catalyst candidates.

Experiments on Au_{25}-based clusters with PET ligands report the HER onset potentials for $PdAu_{24}$, Au_{25}, and $CuAu_{24}$ to be −0.33 V_{SHE}, −0.37 V_{SHE}, and −0.57 V_{SHE} (−0.29, − 0.33, and −0.53 V_{RHE} at pH 0.7), respectively.[26] The order of activity in terms of the measured current density was reported to be $PdAu_{24}(PET)_{18}$ > $Au_{25}(PET)_{18}$ > $CuAu_{24}(PET)_{18}$ at any voltage where all three samples were active.[26] Our computationally determined redox potentials neglect entropic contributions, and errors may arise due to the implicit solvent model, the exchange-correlation functional, and the substitution of PET ligands with smaller methyl groups. Therefore, our values need not necessarily align with the experimentally observed onset potentials. However, if we were to compare our results at voltages such as −0.60 or −0.70 V_{SHE}, as considered in Kumar et al.'s paper, we find the same trend in activity. At such voltages, the Pd-doped cluster exists as $[PdAu_{24}]^{-2}$, while the pure and Cu-doped clusters are stable as $[Au_{25}]^{-1}$ and $[CuAu_{24}]^{-1}$. The first Volmer step on the Pd-doped cluster is barrierless and the most exergonic among the clusters considered. The Au cluster has a very small barrier (0.09 eV) and a favorable reaction energy (−0.49 eV), while the Cu-doped cluster has the least favorable reaction energy (−0.22 eV) and a high barrier of 0.67 eV. In effect, our calculations also suggest the same order of reactivity: $PdAu_{24}$ > Au_{25} > $CuAu_{24}$.

The calculated redox potentials demonstrate that these clusters exist in different charge states under the reaction conditions. Employing the common method of comparing reactivity at a given charge state would lead to a different order of reactivity. For example, on neutral clusters (see q = 1 in Table 2), the reaction barriers would give the order of activity $CuAu_{24}$ > $PdAu_{24}$ > Au_{25} while the reaction energies would give $PdAu_{24}$ > $CuAu_{24}$ > Au_{25}.

ENERGETICS OF A POSSIBLE SECOND VOLMER STEP

Next, we consider the second Volmer step under acidic conditions: $H_3O^+ + [HMAu_{24}(SR)_{18}]^{q}-1 \rightarrow H_2O + [H_2MAu_{24}(SR)_{18}]^{q}$. Here, a second H_3O^+ decomposes into a proton adsorbed on the hydrogenated cluster and a water molecule. This is the precursor to the Tafel step, where two adsorbed H atoms combine to form a hydrogen molecule.

If the clusters are active as homogeneous catalysts in solution, then one should consider the possibility that the proton and electron transfers are not necessarily coupled. In other words, the clusters could follow this sequence upon protonation: $[MAu_{24}]^{q}-2 \rightarrow [HMAu_{24}]^{q}-1 \rightarrow [H_{2M}Au_{24}]^{q}$. This would, of course, depend on the relative rate at which the cluster's charge state can be stabilized at the given potential and the rate of reaction for the second Volmer step. If the clusters are heterogeneous catalysts, as in the experiments by Kumar et al.,[26] they are supported on an electrode which acts as an infinite source or sink of electrons. This allows the clusters to change their charge state while maintaining a constant potential. Therefore, it is important to identify the relevant charge state of the hydrogenated cluster at a given potential. Our calculated redox potentials for the hydrogenated clusters are shown in Table 3.

Table 3. Redox Potentials (V_{SHE}) for $[HMAu_{25}(SR)_{18}]^{q}$ Clusters, Where M = Au, Cu, Pd, and Reduced q = −2, −1, 0, 1, 2

	Redox Potential (V_{SHE})		
redox pair	HAu_{25}	$HCuAu_{24}$	$HPdAu_{24}$
−2/−1	−0.95	−0.81	−1.04
−1/0	−0.70	−0.71	−0.16
0/+1	0.17	0.58	0.10
+1/+2	0.38	0.36	0.37
+2/+3	0.77	0.74	0.69

In general, the qualitative trends in the redox potentials observed with the bare clusters are also seen in the hydrogenated clusters (Table 3). For example, the redox potentials for $[HAu_{25}]$ and $[HCuAu_{24}]$ are similar. Additionally, for each cluster, the charge state with the largest difference between its reduction and oxidation potentials also has the largest HOMO−LUMO gap (q = 0 for HAu_{25} and $HCuAu_{24}$ and q = −1 for $HPdAu_{24}$). Given the unusually large redox potential for $[HCuAu_{24}]^{0} \leftrightarrow [HCuAu_{24}]^{+1}$, we suggest that the redox potentials are sensitive to the position of the dopant and the adsorbed hydrogen atom within the cluster. The Cu is at the center for both q = −2/−1 and 0/+1 redox reactions; however, the adsorbed hydrogen atoms are in different positions. For q = −2/−1, the hydrogen is located at a bridge site between two icosahedral Au atoms, whereas for q = 0/+1, it is at a hollow site binding to the center atom (see Table SI-9). Nevertheless, from the redox potentials given in Table 3, we see that the charge states relevant for HER activity are q =

https://doi.org/10.1021/acscatal.3c01065
ACS Catal. 2023, 13, 8997−9006

0, −1, and −2 for [HAu_{25}] and [$HCuAu_{24}$], and q = 0 and −1 for [$HPdAu_{24}$].

The calculated free energies of the reaction and activation barriers for the second proton adsorption on each cluster for all charges considered are given in Table 4. Here again, q is the overall charge of the system in the reaction, where $[HMAu_{24}]^{q-1}$ becomes $[H_2MAu_{24}]^q$. As shown by the Bader analysis in Figure SI-5, while the H atom already adsorbed on the cluster maintains its neutral charge over the course of the second Volmer step, the second H transferred from H_3O^+ to the cluster loses its positive charge. This confirms that the second proton also gains an electron from the cluster. As was the case for the first Volmer step, the second Volmer step becomes increasingly exergonic; that is, the reaction becomes more energetically favorable as the cluster is reduced from +1 to −2.

Table 4. Free Energies of Activation and Reaction (eV) for a Second Volmer Step: $H_3O^+ + [HMAu_{24}(SR)_{18}]^{q-1} \rightarrow H_2O + [H_2MAu_{24}(SR)_{18}]^q$, Where M = Au, Cu, Pd and q = −1, 0, 1, 2

	Au		Cu		Pd	
q	activation	reaction	activation	reaction	activation	reaction
−1	0.000	−0.470	0.274	−0.349	0.049	−0.747
0	0.000	−0.319	0.096	−0.320	0.653	−0.226
+1	0.562	0.076	0.000	−0.259	0.238	−0.158
+2	0.313	−0.006	0.873	0.343	0.323	−0.027

At 0 V_{SHE}, HAu_{25} exists as $[HAu_{25}]^0$ and the reaction is slightly endothermic with a barrier of 0.56 eV (see q = 1 in Table 4). At potentials below −0.70 V_{SHE} (q = 0 or −1 in Table 4), the reaction becomes thermodynamically favorable and barrierless.

The results for $HCuAu_{24}$ are in high contrast here. This cluster exists as $[HCuAu_{24}]^0$ at 0 V_{SHE} and stabilizes to $[HCuAu_{24}]^{-1}$ and $[HCuAu_{24}]^{-2}$ at −0.71 V_{SHE} and −0.81 V_{SHE}, respectively. The second Volmer step is exergonic for each of these three clusters. As the hydrogenated cluster is reduced from q = 0 to q = −2, the reaction barrier increases slightly from 0 to 0.27 eV. Since the second Volmer step occurs easily, thereby paving the route for a Volmer−Tafel mechanism, the rate-determining step on Cu-doped clusters may be the Tafel or the first Volmer step. For $HPdAu_{24}$, the relevant charge states, 0 and −1, are stable at potential ranges of 0 to −0.16 V_{SHE} and −0.16 to −1.04 V_{SHE}, respectively. $[HPdAu_{24}]^0$ and $[HPdAu_{24}]^{-1}$ (q = +1 and 0 in Table 4) are both energetically favorable toward the second proton adsorption and have barriers of 0.24 and 0.65 eV, respectively.

Given that HER activity is observed for Cu-doped clusters only below −0.57 V_{SHE} (−0.53 V_{RHE} at pH 0.7),[26] the relevant charge states to compare activity toward the second Volmer step are $[HAu_{25}]^0$, $[HCuAu_{24}]^0$, and $[HPdAu_{24}]^{-1}$. While the reaction easily proceeds on the Cu-doped cluster, it is energetically unfavorable on the pure cluster, and both the Pd-doped and pure clusters have significant reaction barriers. This points to the likely fact that, in the case of Au and Pd-doped clusters, the adsorption of the second H is not highly favored and the Volmer−Heyrovsky mechanism may be the preferred route for HER activity.

The significant differences between the first and second proton transfer energetics and the corresponding kinetic barriers demonstrate how sensitive these systems are to the presence and configuration of two adsorbates. This sensitivity appears to agree with the discussion above of the NCs' adsorption energies and HOMO−LUMO gaps.

CONCLUSIONS

We have investigated the effects of doping $[Au_{25}(SR)_{18}]^q$ clusters on their stability, strength of hydrogen adsorption, redox potentials, and efficacy as HER catalysts. We considered single atom Cu and Pd doping and different charge states (q = −2, −1, 0, +1, +2).

Electronic stabilities given by HOMO−LUMO gaps and adsorption energies for 1−3 H atoms were correlated to the clusters' superatomic electron configuration. Generally, clusters corresponding to an $8e^-$ superatom have larger HOMO−LUMO gaps, higher stability, and lower H adsorption energies (stronger binding) than those with other electronic configurations.

The range of potentials of interest to study HER activity under acidic conditions is generally between 0 and −1 V_{SHE}. Based on our calculated redox potentials, the charge states that exist in this range are +1, 0, and −1 for Au_{25} and $CuAu_{24}$, and 0, −1, and −2 for $PdAu_{24}$. Interestingly, the trend observed in the potential of zero charge or the redox potential to reach the cluster with q = 0 agrees with the experimentally observed trend in HER onset potentials:[26] $PdAu_{24}$ > Au_{25} > $CuAu_{24}$.

We computed the free energies of the reaction and kinetic barriers for the first and second Volmer steps under acidic conditions. At −0.6 or −0.7 V_{SHE}, we find that $PdAu_{24}$ exists at q = −2, while Au_{25} and $CuAu_{24}$ exist in a different charge state q = −1. The corresponding reaction energies and kinetic barriers give the following order of activity toward the first Volmer step: $PdAu_{24}$ > Au_{25} > $CuAu_{24}$, the same trend observed experimentally.[26] We find that $PdAu_{24}$ and Au_{25} have reactivity toward the Volmer step that is comparable to that of Pt(111),[28] making them promising HER catalysts.

Our results for the second Volmer step on Au_{25}, $CuAu_{24}$, and $PdAu_{24}$ raise the possibility that these three clusters may not necessarily follow the same mechanism for HER. The adsorption of the second H appears effortless on the Cu-doped cluster, suggesting the Volmer−Tafel mechanism may occur. For the Au and Pd-doped cluster, however, the adsorption of the second H is not favorable, thereby suggesting the Volmer−Heyrovsky mechanism is preferred. Further investigations on the following steps in the HER would help confirm this.

We believe this study to be an improvement to the computational strategies generally employed, where investigations and comparisons are carried out on clusters in their neutral or stable charge state. This work highlights the importance of determining redox potentials and identifying the relevant charge states of a cluster under the electrochemical reaction conditions. Our results confirm that choosing an appropriate dopant can help control the charge state at a given potential, hydrogen adsorption energies, HER activity, and reaction mechanism significantly. This study brings us closer to understanding and developing both computational and experimental strategies to design highly active HER catalysts.

ASSOCIATED CONTENT

Supporting Information

The Supporting Information is available free of charge at https://pubs.acs.org/doi/10.1021/acscatal.3c01065. XYZ files of relevant atomic structures are available at 10.23729/c4c2b15c-3fd6-437b-82eb-8babf3119ee5.

https://doi.org/10.1021/acscatal.3c01065
ACS Catal. 2023, 13, 8997−9006

Details of superatomic electron filling, magnetic moments, results for different dopant positions in cluster, adsorption energies for H, 2H, and 3H at different possible sites, H binding distances for stable geometries and reaction paths, free-energy diagrams for the first and second Volmer steps and Bader analysis for states along the reaction paths (PDF)

AUTHOR INFORMATION

Corresponding Authors

Hannu Häkkinen − *Department of Physics, Nanoscience Center, University of Jyväskylä, FI-40014 Jyväskylä, Finland; Department of Chemistry, Nanoscience Center, University of Jyväskylä, FI-40014 Jyväskylä, Finland;* orcid.org/0000-0002-8558-5436; Email: hannu.j.hakkinen@jyu.fi

Karoliina Honkala − *Department of Chemistry, Nanoscience Center, University of Jyväskylä, FI-40014 Jyväskylä, Finland;* orcid.org/0000-0002-3166-1077; Email: karoliina.honkala@jyu.fi

Authors

Omar López-Estrada − *Department of Chemistry, Nanoscience Center, University of Jyväskylä, FI-40014 Jyväskylä, Finland;* orcid.org/0000-0002-9395-334X

Nisha Mammen − *Department of Physics, Nanoscience Center, University of Jyväskylä, FI-40014 Jyväskylä, Finland;* orcid.org/0000-0002-1550-6333

Laura Laverdure − *Department of Chemistry, Nanoscience Center, University of Jyväskylä, FI-40014 Jyväskylä, Finland*

Marko M. Melander − *Department of Chemistry, Nanoscience Center, University of Jyväskylä, FI-40014 Jyväskylä, Finland;* orcid.org/0000-0001-7111-1603

Complete contact information is available at: https://pubs.acs.org/10.1021/acscatal.3c01065

Notes

The authors declare no competing financial interest.

ACKNOWLEDGMENTS

This work was supported by the Academy of Finland (Grant Nos. 351582, 317739, 351583, 332290, 338228). Computational resources were provided by the CSC-IT Center for Science, Espoo, Finland. The authors thank Prof. Yuichi Negishi for fruitful discussions on the experimental details in ref 22 and Dr. Sami Malola for help regarding the initial cluster structures used in the calculations.

REFERENCES

(1) Rogelj, J.; Schaeffer, M.; Meinshausen, M.; Shindell, D. T.; Hare, W.; Klimont, Z.; Velders, G. J. M.; Amann, M.; Schellnhuber, H. J. Disentangling the effects of CO_2 and short-lived climate forcer mitigation. *Proc. Natl. Acad. Sci. U. S. A.* **2014**, *111*, 16325−16330.

(2) Clack, C. T. M.; et al. Evaluation of a proposal for reliable low-cost grid power with 100% wind, water, and solar. *Proc. Natl. Acad. Sci. U. S. A.* **2017**, *114*, 6722−6727.

(3) Tee, S. Y.; Win, K. Y.; Teo, W. S.; Koh, L.-D.; Liu, S.; Teng, C. P.; Han, M.-Y. Recent Progress in Energy-Driven Water Splitting. *Adv. Sci.* **2017**, *4*, 1600337.

(4) Hu, C.; Zhang, L.; Gong, J. Recent progress made in the mechanism comprehension and design of electrocatalysts for alkaline water splitting. *Energy Environ. Sci.* **2019**, *12*, 2620−2645.

(5) Turner, J. A. Sustainable Hydrogen Production. *Science* **2004**, *305*, 972−974.

(6) Sabatier, P. Hydrogénations et déshydrogénations par catalyse. *Ber. Dtsch. Chem. Ges.* **1911**, *44*, 1984−2001.

(7) Nørskov, J. K.; Bligaard, T.; Logadottir, A.; Kitchin, J. R.; Chen, J. G.; Pandelov, S.; Stimming, U. Trends in the Exchange Current for Hydrogen Evolution. *J. Electrochem. Soc.* **2005**, *152*, J23.

(8) Seh, Z. W.; Kibsgaard, J.; Dickens, C. F.; Chorkendorff, I.; Nørskov, J. K.; Jaramillo, T. F. Combining theory and experiment in electrocatalysis: Insights into materials design. *Science* **2017**, *355*, eaad4998.

(9) Kim, J. H.; Hansora, D.; Sharma, P.; Jang, J.-W.; Lee, J. S. Toward practical solar hydrogen production - an artificial photosynthetic leaf-to-farm challenge. *Chem. Soc. Rev.* **2019**, *48*, 1908−1971.

(10) Zhao, G.; Rui, K.; Dou, S. X.; Sun, W. Heterostructures for Electrochemical Hydrogen Evolution Reaction: A Review. *Adv. Funct. Mater.* **2018**, *28*, 1803291.

(11) Kibsgaard, J.; Chorkendorff, I. Considerations for the scaling-up of water splitting catalysts. *Nat. Energy* **2019**, *4*, 430−433.

(12) Wang, S.; Lu, A.; Zhong, C.-J. Hydrogen production from water electrolysis: role of catalysts. *Nano Convergence* **2021**, *8*, 4.

(13) Govindarajan, N.; Kastlunger, G.; Heenen, H. H.; Chan, K. Improving the intrinsic activity of electrocatalysts for sustainable energy conversion: where are we and where can we go? *Chem. Sci.* **2021**, *13*, 14−26.

(14) Deng, C.; Li, F.; Tang, Q. Electrocatalytic Oxygen Reduction Reaction over the $Au_{22}(L^8)_6$ Nanocluster with Promising Activity: A DFT Study. *J. Phys. Chem. C* **2019**, *123*, 27116−27123.

(15) Wu, Z.; Hu, G.; Jiang, D.-e.; Mullins, D. R.; Zhang, Q.-F.; Allard, L. F.; Wang, L.-S.; Overbury, S. H. Diphosphine-Protected Au_{22} Nanoclusters on Oxide Supports Are Active for Gas-Phase Catalysis without Ligand Removal. *Nano Lett.* **2016**, *16*, 6560−6567.

(16) Sokołowska, K.; Malola, S.; Lahtinen, M.; Saarnio, V.; Permi, P.; Koskinen, K.; Jalasvuori, M.; Häkkinen, H.; Lehtovaara, L.; Lahtinen, T. Towards Controlled Synthesis of Water-Soluble Gold Nanoclusters: Synthesis and Analysis. *J. Phys. Chem. C* **2019**, *123*, 2602−2612.

(17) Shibu, E. S.; Muhammed, M. A. H.; Tsukuda, T.; Pradeep, T. Ligand Exchange of $Au_{25}SG_{18}$ Leading to Functionalized Gold Clusters: Spectroscopy, Kinetics, and Luminescence. *J. Phys. Chem. C* **2008**, *112*, 12168−12176.

(18) Maity, P.; Xie, S.; Yamauchi, M.; Tsukuda, T. Stabilized gold clusters: from isolation toward controlled synthesis. *Nanoscale* **2012**, *4*, 4027−4037.

(19) Srisombat, L.-o.; Park, J.-S.; Zhang, S.; Lee, T. R. Preparation, Characterization, and Chemical Stability of Gold Nanoparticles Coated with Mono-, Bis-, and Tris-Chelating Alkanethiols. *Langmuir* **2008**, *24*, 7750−7754.

(20) Lopez-Acevedo, O.; Kacprzak, K. A.; Akola, J.; Häkkinen, H. Quantum size effects in ambient CO oxidation catalysed by ligand-protected gold clusters. *Nat. Chem.* **2010**, *2*, 329−334.

(21) Hu, G.; Wu, Z.; Jiang, D.-e. Stronger-than-Pt hydrogen adsorption in a Au_{22} nanocluster for the hydrogen evolution reaction. *J. Mater. Chem. A* **2018**, *6*, 7532−7537.

(22) Jin, R.; Li, G.; Sharma, S.; Li, Y.; Du, X. Toward Active-Site Tailoring in Heterogeneous Catalysis by Atomically Precise Metal Nanoclusters with Crystallographic Structures. *Chem. Rev.* **2021**, *121*, 567−648.

(23) Zhang, B.; Chen, J.; Cao, Y.; Chai, O. J. H.; Xie, J. Ligand Design in Ligand-Protected Gold Nanoclusters. *Small* **2021**, *17*, 2004381.

(24) Hu, G.; Tang, Q.; Lee, D.; Wu, Z.; Jiang, D.-e. Metallic Hydrogen in Atomically Precise Gold Nanoclusters. *Chem. Mater.* **2017**, *29*, 4840−4847.

(25) Kwak, K.; Choi, W.; Tang, Q.; Kim, M.; Lee, Y.; Jiang, D.-e.; Lee, D. A molecule-like $PtAu_{24}(SC_6H_{13})_{18}$ nanocluster as an electrocatalyst for hydrogen production. *Nat. Commun.* **2017**, *8*, 14723.

(26) Kumar, B.; Kawawaki, T.; Shimizu, N.; Imai, Y.; Suzuki, D.; Hossain, S.; Nair, L. V.; Negishi, Y. Gold nanoclusters as

electrocatalysts: size, ligands, heteroatom doping, and charge dependences. *Nanoscale* **2020**, *12*, 9969−9979.
(27) Choi, W.; Hu, G.; Kwak, K.; Kim, M.; Jiang, D.-e.; Choi, J.-P.; Lee, D. Effects of Metal-Doping on Hydrogen Evolution Reaction Catalyzed by MAu_{24} and M_2Au_{36} Nanoclusters (M = Pt, Pd). *ACS Appl. Mater. Interfaces* **2018**, *10*, 44645−44653.
(28) Lindgren, P.; Kastlunger, G.; Peterson, A. A. A Challenge to the G ∼ 0 Interpretation of Hydrogen Evolution. *ACS Catal.* **2020**, *10*, 121−128.
(29) Rebollar, L.; Intikhab, S.; Oliveira, N. J.; Yan, Y.; Xu, B.; McCrum, I. T.; Snyder, J. D.; Tang, M. H. Beyond Adsorption" Descriptors in Hydrogen Electrocatalysis. *ACS Catal.* **2020**, *10*, 14747−14762.
(30) Dubouis, N.; Grimaud, A. The hydrogen evolution reaction: from material to interfacial descriptors. *Chem. Sci.* **2019**, *10*, 9165−9181.
(31) Sakaushi, K.; Kumeda, T.; Hammes-Schiffer, S.; Melander, M. M.; Sugino, O. Advances and challenges for experiment and theory for multi-electron multi-proton transfer at electrified solid-liquid interfaces. *Phys. Chem. Chem. Phys.* **2020**, *22*, 19401−19442.
(32) Kauffman, D. R.; Alfonso, D.; Matranga, C.; Ohodnicki, P.; Deng, X.; Siva, R. C.; Zeng, C.; Jin, R. Probing active site chemistry with differently charged Au_{25}^q nanoclusters (q = −1, 0, +1). *Chem. Sci.* **2014**, *5*, 3151−3157.
(33) Melander, M. M.; Kuisma, M. J.; Christensen, T. E. K.; Honkala, K. Grand-canonical approach to density functional theory of electrocatalytic systems: Thermodynamics of solid-liquid interfaces at constant ion and electrode potentials. *J. Chem. Phys.* **2019**, *150*, 041706.
(34) Melander, M. M. Grand canonical ensemble approach to electrochemical thermodynamics, kinetics, and model Hamiltonians. *Curr. Opin. Electrochem.* **2021**, *29*, 100749.
(35) Prats, H.; Chan, K. The determination of the HOR/HER reaction mechanism from experimental kinetic data. *Phys. Chem. Chem. Phys.* **2021**, *23*, 27150−27158.
(36) Exner, K. S.; Sohrabnejad-Eskan, I.; Over, H. A Universal Approach To Determine the Free Energy Diagram of an Electrocatalytic Reaction. *ACS Catal.* **2018**, *8*, 1864−1879.
(37) Shinagawa, T.; Garcia-Esparza, A. T.; Takanabe, K. Insight on Tafel slopes from a microkinetic analysis of aqueous electrocatalysis for energy conversion. *Sci. Rep.* **2015**, *5*, 13801.
(38) Kronberg, R.; Laasonen, K. Reconciling the experimental and computational hydrogen evolution activities of Pt(111) through DFT-based constrained MD simulations. *ACS Catal.* **2021**, *11*, 8062−8078.
(39) Tofanelli, M. A.; Salorinne, K.; Ni, T. W.; Malola, S.; Newell, B.; Phillips, B.; Häkkinen, H.; Ackerson, C. J. Jahn-Teller effects in $Au_{25}(SR)_{18}$. *Chem. Sci.* **2016**, *7*, 1882−1890.
(40) Mortensen, J. J.; Hansen, L. B.; Jacobsen, K. W. Real-space grid implementation of the projector augmented wave method. *Phys. Rev. B* **2005**, *71*, 035109.
(41) Enkovaara, J.; et al. Electronic structure calculations with GPAW: A real-space implementation of the projector augmented-wave method. *J. Phys.: Condens. Matter* **2010**, *22*, 253202.
(42) Hjorth Larsen, A.; Jørgen Mortensen, J.; Blomqvist, J.; Castelli, I. E; Christensen, R.; Dułak, M.; Friis, J.; Groves, M. N; Hammer, B.ør.; Hargus, C.; et al. The Atomic Simulation Environment—A Python library for working with atoms. *J. Phys.: Condens. Matter* **2017**, *29*, 273002.
(43) Perdew, J.; Burke, K.; Ernzerhof, M. Generalized Gradient Approximation Made Simple. *Phys. Rev. Lett.* **1996**, *77*, 3865−3868.
(44) Tkatchenko, A.; Scheffler, M. Accurate Molecular Van Der Waals Interactions from Ground-State Electron Density and Free-Atom Reference Data. *Phys. Rev. Lett.* **2009**, *102*, 073005.
(45) Held, A.; Walter, M. Simplified continuum solvent model with a smooth cavity based on volumetric data. *J. Chem. Phys.* **2014**, *141*, 174108.
(46) Trasatti, S. The Absolute Electrode Potential: An Explanatory Note. *Pure Appl. Chem.* **1986**, *58*, 955−966.
(47) Henkelman, G.; Jónsson, H. Improved tangent estimate in the nudged elastic band method for finding minimum energy paths and saddle points. *J. Chem. Phys.* **2000**, *113*, 9978−9985.
(48) Henkelman, G.; Uberuaga, B. P.; Jónsson, H. A climbing image nudged elastic band method for finding saddle points and minimum energy paths. *J. Chem. Phys.* **2000**, *113*, 9901−9904.
(49) Henkelman, G.; Arnaldsson, A.; Jónsson, H. A fast and robust algorithm for Bader decomposition of charge density. *Comput. Mater. Sci.* **2006**, *36*, 354−360.
(50) Negishi, Y.; Munakata, K.; Ohgake, W.; Nobusada, K. Effect of Copper Doping on Electronic Structure, Geometric Structure, and Stability of Thiolate-Protected Au_{25} Nanoclusters. *J. Phys. Chem. Lett.* **2012**, *3*, 2209−2214.
(51) Hossain, S.; Suzuki, D.; Iwasa, T.; Kaneko, R.; Suzuki, T.; Miyajima, S.; Iwamatsu, Y.; Pollitt, S.; Kawawaki, T.; Barrabés, N.; Rupprechter, G.; Negishi, Y. Determining and Controlling Cu-Substitution Sites in Thiolate-Protected Gold-Based 25-Atom Alloy Nanoclusters. *J. Phys. Chem. C* **2020**, *124*, 22304−22313.
(52) Walter, M.; Akola, J.; Lopez-Acevedo, O.; Jadzinsky, P. D.; Calero, G.; Ackerson, C. J.; Whetten, R. L.; Grönbeck, H.; Häkkinen, H. A unified view of ligand-protected gold clusters as superatom complexes. *Proc. Natl. Acad. Sci. U. S. A.* **2008**, *105*, 9157−9162.
(53) Kang, X.; Chong, H.; Zhu, M. $Au_{25}(SR)_{18}$: the captain of the great nanocluster ship. *Nanoscale* **2018**, *10*, 10758−10834.
(54) Negishi, Y.; Kurashige, W.; Niihori, Y.; Iwasa, T.; Nobusada, K. Isolation, structure, and stability of a dodecanethiolate-protected Pd_1Au_{24} cluster. *Phys. Chem. Chem. Phys.* **2010**, *12*, 6219−6225.
(55) Niihori, Y.; Kurashige, W.; Matsuzaki, M.; Negishi, Y. Remarkable enhancement in ligand-exchange reactivity of thiolate-protected Au_{25} nanoclusters by single Pd atom doping. *Nanoscale* **2013**, *5*, 508−512.
(56) Sels, A.; Barrabés, N.; Knoppe, S.; Bürgi, T. Isolation of atomically precise mixed ligand shell $PdAu_{24}$ clusters. *Nanoscale* **2016**, *8*, 11130−11135.
(57) Zhou, M.; Qian, H.; Sfeir, M. Y.; Nobusada, K.; Jin, R. Effects of single atom doping on the ultrafast electron dynamics of $M_1Au_{24}(SR)_{18}$ (M = Pd, Pt) nanoclusters. *Nanoscale* **2016**, *8*, 7163−7171.
(58) Tian, S.; Liao, L.; Yuan, J.; Yao, C.; Chen, J.; Yang, J.; Wu, Z. Structures and magnetism of mono-palladium and mono-platinum doped $Au_{25}(PET)_{18}$ nanoclusters. *Chem. Commun.* **2016**, *52*, 9873−9876.
(59) Antonello, S.; Perera, N. V.; Ruzzi, M.; Gascón, J. A.; Maran, F. Interplay of Charge State, Lability, and Magnetism in the Molecule-like $Au_{25}(SR)_{18}$ Cluster. *J. Am. Chem. Soc.* **2013**, *135*, 15585−15594.
(60) Isegawa, M.; Neese, F.; Pantazis, D. A. Ionization Energies and Aqueous Redox Potentials of Organic Molecules: Comparison of DFT, Correlated ab Initio Theory and Pair Natural Orbital Approaches. *J. Chem. Theory Comput.* **2016**, *12*, 2272−2284.
(61) Ooka, H.; Nakamura, R. Shift of the Optimum Binding Energy at Higher Rates of Catalysis. The. *J. Phys. Chem. Lett.* **2019**, *10*, 6706−6713.
(62) Zeradjanin, A. R.; Narangoda, P.; Masa, J.; Schlögl, R. What Controls Activity Trends of Electrocatalytic Hydrogen Evolution Reaction?-Activation Energy Versus Frequency Factor. *ACS Catal.* **2022**, *12*, 11597−11605.

https://doi.org/10.1021/acscatal.3c01065
ACS Catal. 2023, 13, 8997−9006